Front. Chem. Sci. Eng. 2023, 17(5): 525−535
https://doi.org/10.1007/s11705-022-2232-5

RESEARCH ARTICLE

Floret-like Fe–N_x nanoparticle-embedded porous carbon superstructures from a Fe-covalent triazine polymer boosting oxygen electroreduction

Yong Zheng (✉)[1,4], Mingjin Li[1], Yongye Wang[1], Niu Huang[1,4], Wei Liu[1,4], Shan Chen[2], Xuepeng Ni[2], Kunming Li[2], Siwei Xiong[3], Yi Shen[5], Siliang Liu[6], Baolong Zhou[7], Niaz Ali Khan (✉)[8], Liqun Ye (✉)[1,4], Chao Zhang (✉)[2], Tianxi Liu[2]

1 College of Materials and Chemical Engineering, Key Laboratory of Inorganic Nonmetallic Crystalline and Energy Conversion Materials, China Three Gorges University, Yichang 443002, China
2 State Key Laboratory for Modification of Chemical Fibers and Polymer Materials, College of Materials Science and Engineering, Donghua University, Shanghai 201620, China
3 College of Materials Science and Engineering, Hubei Key Laboratory for New Textile Materials and Applications, Wuhan Textile University, Wuhan 430200, China
4 Hubei Three Gorges Laboratory, Yichang 443007, China
5 College of Environment, Zhejiang University of Technology, Hangzhou 310032, China
6 College of Light-Textile Engineering and Art, Anhui Agricultural University, Hefei 230036, China
7 School of Pharmacy, Weifang Medical University, Weifang 261053, China
8 Key Laboratory of Textile Fiber and Products (Wuhan Textile University), Ministry of Education, Wuhan 430200, China

Abstract Fe–N_x nanoparticles-embedded porous carbons with a desirable superstructure have attracted immense attention as promising catalysts for electrochemical oxygen reduction reaction. Herein, we employed Fe-coordinated covalent triazine polymer for the fabrication of Fe–N_x nanoparticle-embedded porous carbon nanoflorets (Fe/N@CNFs) employing a hypersaline-confinement-conversion strategy. Presence of tailored N types within the covalent triazine polymer interwork in high proportions contributes to the generation of Fe/N coordination and subsequent Fe–N_x nanoparticles. Owing to the utilization of NaCl crystals, the resultant Fe/N@CNF-800 which was generated by pyrolysis at 800 °C showed nanoflower structure and large specific surface area, which remarkably suppressed the agglomeration of high catalytic active sites. As expect, the Fe/N@CNF-800 exhibited unexpected oxygen reduction reaction catalytic performance with an ultrahigh half-wave potential (0.89 V vs. reversible hydrogen electrode), a dominant $4e^-$ transfer approach and great cycle stability (> 92% after 100000 s). As a demonstration, the Fe/N-PCNF-800-assembled zinc–air battery delivered a high open circuit voltage of 1.51 V, a maximum peak power density of 164 $mW \cdot cm^{-2}$, as well as eminent rate performance, surpassing those of commercial Pt/C. This contribution offers a valuable avenue to exploit efficient metal nanoparticles-based carbon catalysts towards energy-related electrocatalytic reactions and beyond.

Keywords Fe–N_x nanoparticles, hypersaline-confinement conversion, floret-like carbon, covalent triazine polymers, oxygen reduction reaction

1 Introduction

High theoretical energy density and environmentally benign nature make metal–air (oxygen) batteries and fuel cells as ideal sustainable energy conversion technologies [1–5]. However, their commercial applications have been greatly limited due to slow kinetic procedure of cathodic oxygen reduction reaction (ORR) [6]. Until now, platinum-based (20 wt % Pt/C) catalysts are the mainly available commercial ORR catalyst owing to their ultrahigh electrocatalytic activity but high-cost and insufficient stability severely preclude their commercialization process [7,8]. Thus, it is imperative to search for alternative ORR electrocatalysts which are efficient, stable and inexpensive.

Received June 6, 2022; accepted August 9, 2022

E-mails: zhengyong@ctgu.edu.cn (Zheng Y.), niaz2mn@hotmail.com (Khan N. A.), lqye@ctgu.edu.cn (Ye L.), czhang@dhu.edu.cn (Zhang C.)

Over the last few decades, considerable efforts have been put forward for the search of advanced and feasible materials with enhanced ORR electrocatalytic performance. Among them, Fe and N co-doped carbon (Fe–N–C) materials have been found to be promising as competitive ORR electrocatalysts as a consequence of their satisfactory electrocatalytic performance and abundant resources. Recently, theoretical and experimental studies have suggested ultrahigh intrinsic ORR electrocatalytic behavior of Fe–N–C composites in alkaline electrolyte [9]. Great progress has been made in the preparation of Fe–N–C catalysts via elaborate screening of the precursors and optimization of the pyrolytic procedures [10,11]. Traditionally, fabrication of these electrocatalysts is carried out by carbonization of the precursor mixture containing C/N/Fe elements under rational pyrolysis temperatures [12]. However, poor morphology control results in unsatisfied ORR catalytic activity obtained via such simple physical mixing pyrolysis routes [13]. As a feasible solution, flower-like carbon microstructures have been of particular interest in the field of corresponding energy conversion reactions [14,15]. The three dimensional (3D) nanoflowers assembled by two dimensional nanosheets have plethora of exposed active sites, thus facilitating the chemisorption and activation of reactant molecules on the catalyst surface [16]. Besides, the electron-transportation can be accelerated through the unique interconnected nanopetals available due to unique morphology which results in excellent electrocatalytic activity [17]. In addition to the ideal microscopic morphology, size of the catalytic active moieties also has great influence on their durability [18–20]. According to previous reports, decreasing size of the Fe–N–C nanomaterials increases the electrocatalytic performance but also impacts their durability in a negative way [21]. In this regard, nanoparticles can balance the durability and catalytic activity due to their unique geometry, electronic structures and large surface-volume ratio [22]. Consequently, homogeneously distributed Fe–N_x nanoparicles within a nanoflower microstructure is particularly desirable for improving the ORR electrocatalytic behavior of Fe–N–C catalysts. Covalent triazine polymers, as a kind of available porous organic polymer, have rich N-containing groups with strong complexation ability to Fe cation and would be a suitable precursor for the preparation of functional Fe–N–C catalysts [23]. In the recent years, various nanostructured carbon catalysts derived from coordinated covalent triazine polymers (CTPs, carbon nanosheets [24], carbon nanotubes [25], carbon nanospheres [26,27], etc.) have been widely studied. Thus, the rational pyrolysis of Fe-CTPs provides a great platform for the preparation of iron nanoparticle-embedded carbon catalysts with unique flower-like nanostructures but is yet to be reported.

Inspired from the above considerations, herein, we designed a hypersaline-confinement graphitization of Fe-CTP into floret-like Fe–N–C materials containing abundant Fe–N_x nanoparticles catalytic centers for the ORR. Strong complexation of Fe ions with pyridinic-N in the CTP framework can accelerate the formation of uniformly distributed Fe–N_x active sites. Under high temperature pyrolysis, the NaCl crystals melt to induce the generation of nanosheets morphology through capillarity force when the graphitization of carbon takes place [28]. Accordingly, Fe–N_x nanoparticle-embedded porous carbon nanofloret (Fe/N@CNF) with floret-like porous nanostructure is generated during the hypersaline-mediated pyrolysis, which is beneficial for the stabilization of Fe–N_x active centers. The as-produced Fe/N@CNF-800 exhibits large specific surface areas (~673.2 $m^2 \cdot g^{-1}$), high N and Fe contents (4.84 and 0.99 at %, respectively). The optimal Fe/N@CNF-800 presents superb ORR electrocatalytic activity under both alkaline and acidic conditions. Moreover, as expected, the performance of the as-constructed zinc–air batteries were also highly improved.

2 Experimental

2.1 Synthesis of Fe-CTP

The Fe-CTP precursor was prepared by a step-wise polymerization with the monomers of piperazine and cyanuric chloride in the present of iron(III) chloride. At first, 1.59 g of piperazine, 2.20 g of cyanuric chloride and 0.15 g iron(III) chloride were dissolved in 250 mL of acetonitrile to generate a uniform system. After that, 5 mL of triethylamine reagent was injected into the solution and then transferred to a reflux bottle. Subsequently, the stirring mixture reacted at three temperature stages, namely, at ~0 °C for 2 h, ~25 °C for 4 h, and ~90 °C for 12 h. Finally, the resultant brownish precipitate was filtered and washed with excess acetone, ethanol, and water several times, and dried in vacuum at 70 °C overnight. The final sample was denoted as Fe-CTP.

2.2 Synthesis of Fe/N@CNF-T (T represents the synthetic temperature)

Typically, 1.2 g of Fe-CTP powder was uniformly dispersed in 25 mL of saturated NaCl solution. Upon lyophilization, the powder mixture (denoted as Fe-CTP@NaCl) was pyrolyzed at different temperature (T = 700, 800, and 900 °C) with a heating rate of 2 °C·min^{-1} for 2 h in an inert atmosphere. After cooling to room temperature naturally, the resultant black samples were washed with 0.5 mol·L^{-1} H_2SO_4 under vigorous stirring and then dried at 60 °C overnight to obtain Fe/N@CNFs samples.

3 Results and discussion

The scheme for fabrication of Fe/N@CNFs nanoarchitecture is illustrated in Fig. 1. Firstly, one-pot polycondensation and coordination was used for the synthesis of Fe-CTP precursor by using cyanuric chloride and piperazine as monomers, triethylamine as acid-binding agent, and $FeCl_3$ as coordination metal salt. The Fe-CTP was obtained after reaction as an insoluble dark brown powder. Figure 1 presents the chemical composition of Fe-CTP with favorable Fe/N coordination between Fe and N atoms. Afterward, the produced brown powder was lyophilized after uniformly dispersing in a saturated NaCl solution. The obtained sample was thermally treated at various temperatures (700, 800 and 900 °C) under Ar atmosphere, followed by leaching using 0.5 mol·L^{-1} H_2SO_4 solution to obtain the Fe/N@CNF-T catalysts.

At first, cross polarization-magic angle spinning ^{13}C nuclear magnetic resonance spectrum was used to demonstrate the chemical structure of CTP. Peaks at 42.7 and 159.3 ppm are displayed in Fig. S1 (cf. Electronic Supplementary Material, ESM), which can be ascribed to the sp^3 carbons in piperazine rings and the sp^2 carbons in triazine rings, respectively. This result manifested the successful synthesis of CTP frameworks through polycondensation. In addition, the presence of indicated peaks at 1300, 1440, and 1520 cm^{-1} in the Fourier-transform infrared spectrum of CTP indicated the presence of triazine rings in CTP matrix (Fig. S2, cf. ESM) [30]. Simultaneously, the disappearance of the signal at 850 cm^{-1} illustrates the consumption of C–Cl bonds, thus affirming the successful formation of CTP network via nucleophilic substitution [31]. Additionally, a peak at 1097 cm^{-1} corresponding to typical Fe/N vibration is present in the Fe-CTP as shown in Fig. S2(b), confirms the successful Fe/N coordination within the CTP [15]. Individual Fe–N_x active sites could be isolated after pyrolysis due to stable Fe-coordinated structure of the CTP [32]. Moreover, the presence of pyridinic-N in Fe-CTP framework facilitates the generation of graphitic-N, pyridinic-N and Fe–N_x species within the resultant Fe/N@CNFs, which are conducive for the improvement of ORR electrocatalytic performance [33]. We assume that the weight loss of complex precursors which is a serious problem during the preparation of Fe-N-based carbon materials via traditional pyrolysis method is prevented due to the presence of NaCl salts which act as confinement media [28]. Thermogravimetric analysis was carried out to check the thermal stability of the corresponding precursors. As demonstrated in Fig. S3 (cf. ESM), due to the introduction of NaCl crystals into the precursor systems, corresponding decrease of precursor weight was remarkably reduced after pyrolysis as a consequence of the significant sealing effect of NaCl crystals on the surface of Fe-CTP [33]. This encapsulation effect prevented large loss of Fe/N coordination components and other N containing intermediates during high temperature heating, which resulted in the formation of high-density catalytic sites [34].

Morphology of the obtained catalysts was investigated by scanning electron microscopy (SEM) and transmission electron microscopy (TEM). The SEM pictures of Fe-CTP complexes are shown in Fig. S4 (cf. ESM), which exhibits random stacked nanosheet aggregates like morphology. Meanwhile, the effect of NaCl salt and different pyrolytic temperatures on the morphological evolution of Fe/N@CNFs affected was also investigated. Morphology of the Fe/N@CNFs samples after carbonization was found to be nanosheets-assembled nanoflorets, demonstrating the role of NaCl crystals as a medium for the formation of nanoflorets upon pyrolysis (Fig. S5, cf. ESM). Importantly, while the Fe/N@CNF-700 exhibits weak connections between isolated nanoflorets, a nanoflower structure with definite nanosheet assemblies

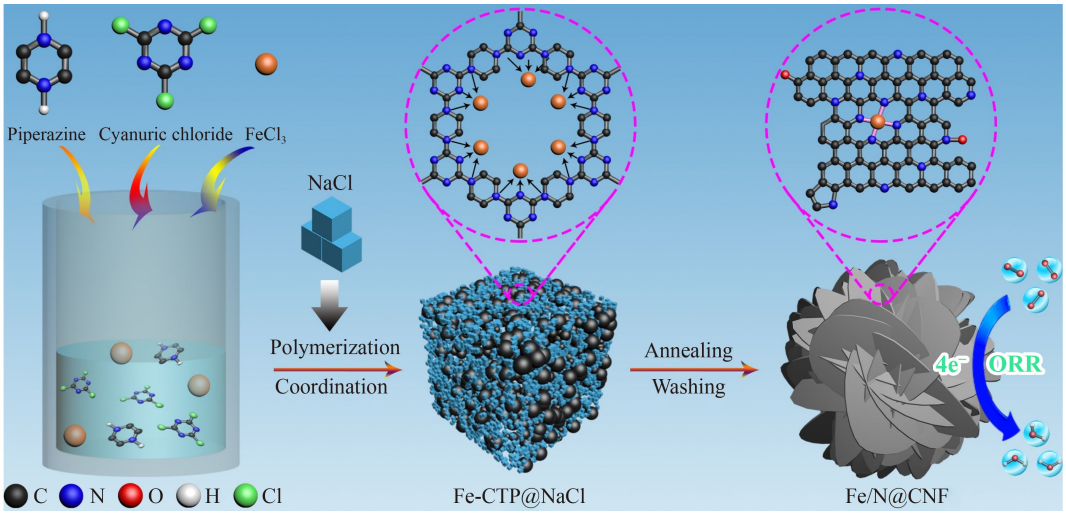

Fig. 1 Schematic synthesis route of Fe/N@CNFs.

was displayed by Fe/N@CNF-800 (Figs. S5(a–f)). Further increase of pyrolysis temperature results in severe agglomerations of the nanoflowers structure which leads to drastic reduction of specific surface areas and exposed active sites (Figs. S5(g–i)). Thus, in order to generate nanostructures with appropriate morphology and surface area which will be beneficial to ORR electrocatalytic activity, optimized pyrolysis temperature of 800 °C is essential [35].

TEM images of Fe/N@CNF-800 indicate a 3D CNF microarchitecture with regular-assembled nanosheets (Fig. 2). As can be seen in Figs. 2(a) and 2(b), individual nanoflorets have effective connection between them which can provide outstanding electroconductivity during ORR process [31]. Importantly, the carbon interwork is found to possess a number of Fe–N_x nanoparticles well-dispersed within the structure (Fig. 2(c)). As shown in the inset of Fig. 2(c), their size ranges from ~2–4 nm with the average size being ~2.8 nm. Moreover, the elemental compositions of Fe/N@CNF-800 were measured by TEM and energy-dispersive X-ray spectroscopy (EDS) elemental mappings. As presented in Fig. 2(d), there is simultaneous and homogenous co-existence of C, N and Fe elements in the carbon framework, which confirms the successful doping of Fe and N elements. Presence of several obvious lattice fringes in the corresponding high-resolution TEM (HRTEM) image demonstrates that the catalyst is graphitic carbon material (Fig. S6, cf. ESM) [36]. Notably, these curved lattice fringes indicate relatively low crystallization owing to the existence of active defects and heteroatoms in the carbon frameworks, which can synergistically boost ORR activity [37].

X-ray diffraction measurement was carried out to characterize the phase composition of Fe/N@CNFs pyrolyzed at different temperatures. Presence of two broad patterns located at 26° and 44° attributed to the diffraction of (002) and (010) lattice planes of graphitic carbon, respectively, can be seen in Fig. S7 (cf. ESM) [36]. These results indicate the conversion of precursor complexes into amorphous carbon after carbonization [28]. In addition, the peaks at 44.6°, 64.8°, and 81.7° can be ascribed to metallic Fe [26]. Physical characterization of Fe/N@CNFs is also provided in Fig. 3 to further show the structural features of Fe/N@CNFs. The characteristic peaks at 1350 and 1590 cm^{-1} in the Raman spectra signify the presence of D and G bands (Fig. 3(a)), corresponding to the disorder and crystallinity of sp^2 hybrid carbon structure, respectively [38]. Moreover, with increasing pyrolysis temperature, there is a decrease of the intensity ratio of I_D/I_G which indicates increasing degree of graphitization of the carbon lattice. The conductivity of as-obtained samples enhances due to increased graphitization of the carbon backbone.

To further confirm the chemical bonding of Fe and N in the derived carbon catalysts, XPS measurements were conducted. The XPS survey spectra of Fe/N@CNFs catalysts affirm the existence of C, Fe, N and O elements, with the corresponding contents of N and Fe elements in the Fe/N@CNF-800 obtained to be 4.84 and 0.99 at %, respectively (Fig. S8 and Table S1, cf. ESM). The doping efficiency of Fe and N elements can be synergistically improved due to the selection of Fe-CTP precursor and the strategy of hypersaline confinement conversion. The high-resolution C 1s spectra (Fig. S9, cf. ESM) of Fe/N@CNF-800 can be deconvoluted into three peaks corresponding to C=C (284.8 eV), C–N/C–C (285.8 eV), and C–O/C=O (287–291 eV) [39]. Deconvolution of the high-resolution N 1s spectra of Fe/N @CNF-800 (Fig. 3(b)) resulted in four peaks, located at 398.8 (Fe–N/pyridinic-N), 400.1 (pyrrolic-N), 401.4 (graphitic-N), and 403.9 eV (quaternary-N) [39]. The plausible bonding schemes of N atom in Fe/N@CNF-800 are

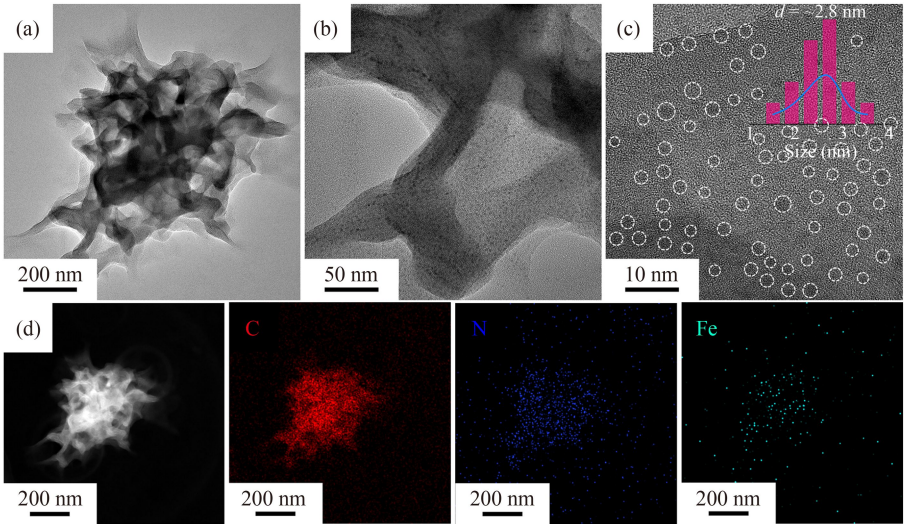

Fig. 2 (a, b) TEM images of Fe/N@CNF-800; (c) HRTEM images of Fe/N@CNF-800; (d) TEM-EDS elemental mapping of Fe/N@CNF-800 for C, N and Fe, respectively.

shown in Fig. 3(c). In a conclusive manner, the Fe–N_x catalytic active center embedded in carbon backbone is obtained via coordination of pyridinic-N with centric Fe atoms. By significantly affecting the charge density of adjacent carbon atoms, the ORR performance and durability are enhanced by the pyrrolic-N atoms [40]. The contents of various N species were determined by integrating the peak areas of corresponding N-types (Fig. S10, cf. ESM). In all the studied catalysts, Fe–N/pyridinic-N and graphitic-N are the main components and are considered as the powerful ORR catalytic sites. The high-resolution XPS spectrum of Fe 2p displays two peaks at around 711.4 and 724.6 eV, which belong to the Fe–N configuration (Fig. 3(d)), suggesting uniform distribution of all Fe species in Fe/N@CNF-800 catalyst. Moreover, the peaks at 714.9 and 729.1 eV are assigned to the satellite peaks of Fe atom [9]. No other peaks were observed which can be attributed to other types of iron and thus manifesting the uniform atomic Fe–N–C state.

N_2 adsorption–desorption measurements were carried out to understand the nature of pores of the as synthesized samples. As shown in Fig. S11 (cf. ESM), the co-existence of mesopores and micropores in the Fe-CTP precursor framework was confirmed from the N_2 sorption/desorption isotherms and corresponding pore size distribution curve. The corresponding N_2 adsorption/desorption profile of Fe/N@CNFs was also obtained to get insight into the change of surface area and nature of pores after carbonization. All the Fe-CTP derived carbon catalysts demonstrated the coexistence of micropores and mesopores as represented by an obvious type-H_4 isotherm in high-pressure areas and a type-H_1 in low-pressure areas [25]. The Brunauer–Emmett–Teller (BET) specific surface area was calculated from these obtained curves. The BET surface area of Fe/N@CNF-800 was found to be ~673.2 $m^2 \cdot g^{-1}$, which was larger than that of other Fe/N@CNFs (Table 1). Thanks to both the hierarchical porous structures and large BET value can result in more exposed active sites and favorable mass/electron transfer

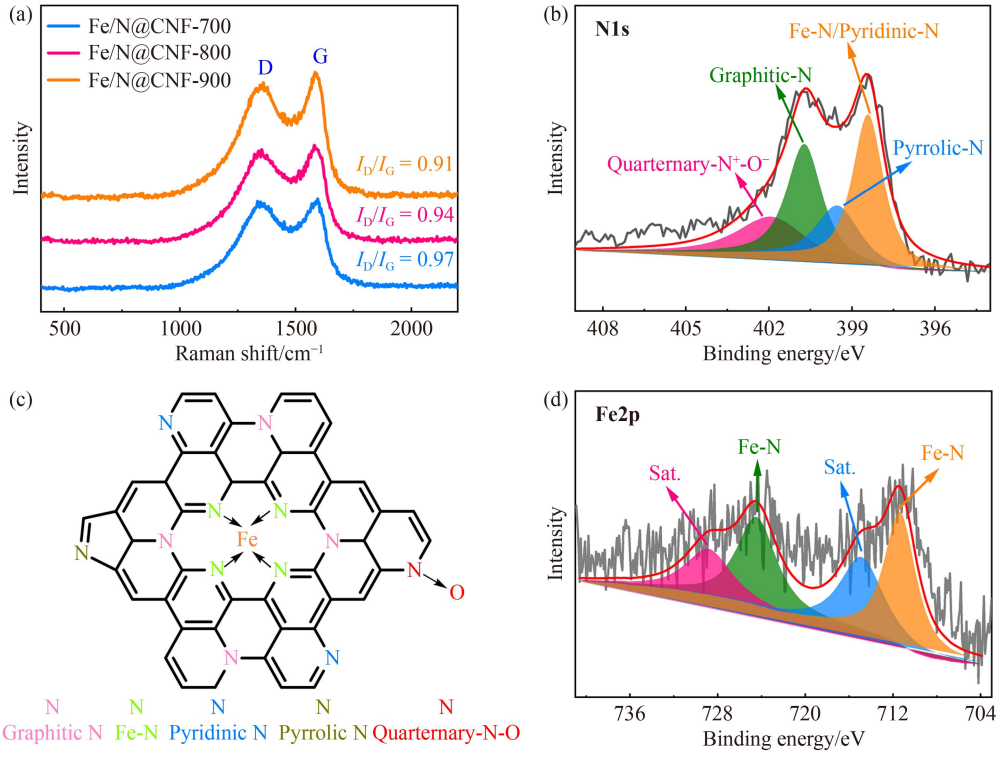

Fig. 3 (a) Raman spectra (1350 and 1590 cm^{-1}) of the Fe/N@CNFs; (b) high-resolution N 1s X-ray photoelectron spectroscopic (XPS) spectra of Fe/N@CNF-800; (c) illustration of N species in the carbon framework of Fe/N@CNF-800; (d) high-resolution Fe 2p XPS spectra of Fe/N@CNF-800.

Table 1 Summary of BET surface area and pore volume for Fe/N@CNFs samples

Sample	BET surface area/($m^2 \cdot g^{-1}$)	Micropore volume/($mL \cdot g^{-1}$)	Mesopore volume/($mL \cdot g^{-1}$)	Total pore volume/($mL \cdot g^{-1}$)
Fe-CTP	133.9	0.073	0.158	0.231
Fe/N@CNF-700	463.0	0.248	0.188	0.436
Fe/N@CNF-800	673.2	0.326	0.161	0.487
Fe/N@CNF-900	382.9	0.181	0.133	0.314

during the ORR [31]. Furthermore, the existence of micropores in Fe/N@CNF-800 can be verified from the pore size distribution (Fig. S12, cf. ESM). This result further confirmed that the Fe-CTP having abundant Fe/N heteroatoms can indeed be considered as a desired precursor for the synthesis of Fe–N–C catalysts with unique microstructure and abundant pores.

The electrocatalytic ORR activities of Fe/N@CNFs were investigated and compared with the Pt/C catalysts in 0.1 mol·L^{-1} KOH aqueous solution (Fig. 4). Cyclic voltammetry (CV) was first employed to determine the ORR performance of the samples. As indicated in Fig. 4(a), no typical peaks can be observed in N_2-saturated 0.1 mol·L^{-1} KOH electrolyte for both Fe/N@CNF-800 and commercial Pt/C catalysts, whereas in O_2-saturated alkaline environment a distinct reduction peak can be observed. Notably, more positive oxygen reduction peak is exhibited by the Fe/N@CNF-800 compared to that of the Pt/C catalyst, certifying higher intrinsic ORR catalytic activity for Fe/N@CNF-800 [41]. Furthermore, corresponding linear sweep voltammetry (LSV) measurements were also carried out under O_2-saturated 0.1 mol·L^{-1} KOH condition (Fig. 4(b)). The onset potential (E_{onset}) and half-wave potential ($E_{1/2}$) of Fe/N@CNF-800 were 1.02 and 0.89 V vs. RHE (reversible hydrogen electrode), respectively, which are more positive than the respective values of Fe/N@CNF-700 (0.95 and 0.82 V), Fe/N@CNF-900 (0.98 and 0.87 V) and commercial Pt/C catalyst (1.01 and 0.86 V). This result reflects the critical role played by the calcination temperature during the synthesis of catalyst. Optimal balance between Fe–N_x, graphitic-N and pyridinic-N active sites can be obtained via appropriate choice of pyrolysis temperature which will subsequently improve the ORR performance greatly. Furthermore, the ORR activity of Fe/N@CNF-800 also was found to exceed most of the recent metal-based carbon electrocatalysts (Table S2, cf. ESM). Moreover, the limiting current density of Fe/N@CNF-800 is also superior to that of commercial Pt/C under identical conditions owing to the high-density active centers and fast mass/electron/ions transport of Fe/N@CNF-800 [42]. The LSV curves of Fe/N@CNF-800 were also measured at varying sweeping rates to gain insights into the dynamics of ORR (Fig. 4(c)). Increasing sweeping rate results in increasing diffusion current thanks to the shorter diffusion distance. The inset of Fig. 4(c) presents the linear Koutecky–Levich (K–L) curves at various potentials. Based on the corresponding K–L equations, the average electron transfer number (n) was calculated to be 3.97–4.00 (Fig. 4(d)), demonstrating an admirable 4e$^-$ reduction pathway on Fe/N@CNF-800 [43]. These obtained results demonstrate the significant progress made in the study of high-efficiency transition metal/carbon-based catalyst for replacing precious metal electrocatalysts. N_2 sorption slope can be employed to evaluate the kinetics process of the ORR. The Fe/N@CNF-800 displays smaller Tafel slope (58 mV·dec^{-1}) than that of commercial Pt/C catalyst (83 mV·dec^{-1}), verifying the faster ORR dynamic process of Fe/N@CNF-800 catalyst (Fig. S13, cf. ESM) [7]. Furthermore, rotation ring disk electrode was conducted to monitor the generation of H_2O_2 and calculate electron-transfer number value during

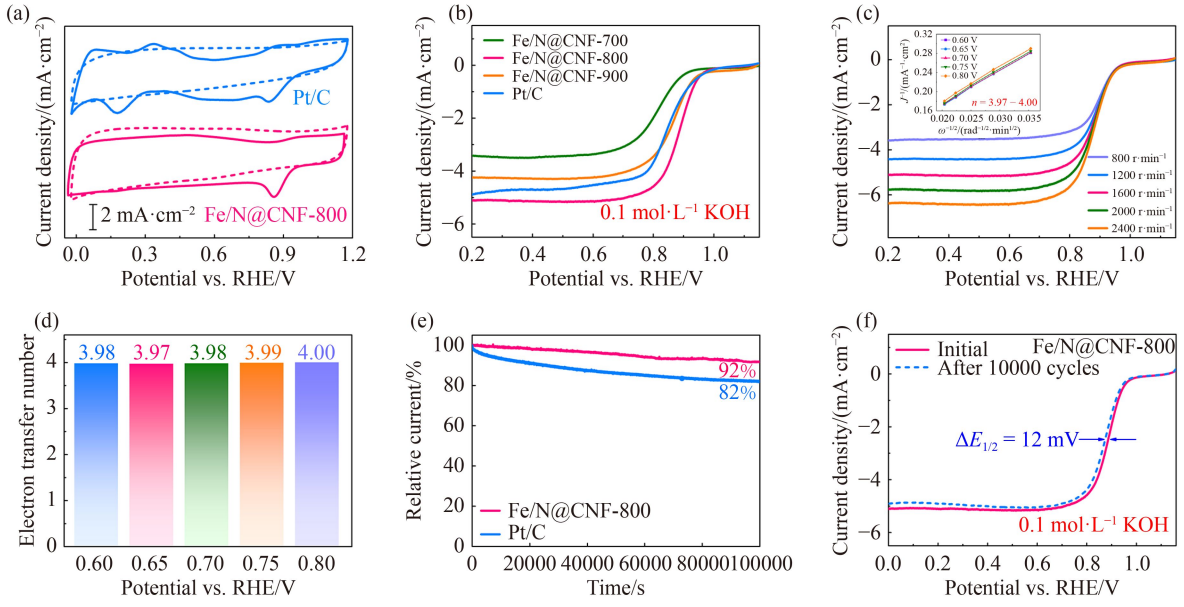

Fig. 4 (a) CV curves of Fe/N@CNF-800 and Pt/C catalysts in N_2- and O_2-saturated 0.1 mol·L^{-1} KOH electrolyte, respectively; (b) LSV curves of the Fe/N@CNFs and Pt/C catalysts, respectively; (c) LSV curves of Fe/N@CNF-800 catalyst at various rotating speeds, inset of (c) is K–L plots of Fe/N@CNF-800 catalyst at various potentials; (d) the n of Fe/N@CNF-800 catalysts calculated from corresponding K–L equation; (e) chronoamperometric responses of Fe/N@CNF-800 and Pt/C catalysts in O_2-saturated 0.1 mol·L^{-1} KOH at 0.664 V, respectively; (f) the LSV curves of Fe/N@CNF-800 before and after 10000 CV cycles.

ORR process. The H_2O_2 yield of Fe/N@CNF-800 was below 5% in the 0.2–0.8 V potential range. Additionally, Fe/N@CNF-800 also possessed the highest electron-transfer number (3.84–3.99), higher than that of commercial Pt/C catalyst (Fig. S14, cf. ESM). The corresponding *i*–*t* curves were also used to study the methanol resistance of Fe/N@CNF-800 and commercial Pt/C catalyst in 0.1 mol·L^{-1} KOH electrolyte. Impressively, the current density of Fe/N@CNF-800 hardly change after adding 1 mol·L^{-1} methanol into the testing electrolyte at 200 s, whereas a sharp decline emerges for Pt/C catalyst (Fig. S15, cf. ESM). These results assert the great methanol resistance of Fe/N@CNF-800, which provides a great platform for the synthesis of ORR catalysts with high methanol tolerance. Stability is another key parameter for the ORR catalyst in practical applications. The stability of Fe/N@CNF-800 was tested by LSV technique in O_2-saturated 0.1 mol·L^{-1} KOH electrolyte [44]. As presented in Fig. 4(e), the current density of Fe/N@CNF-800 maintains ~92% after 100000 s continuous test, outperforming the ~82% of commercial Pt/C catalyst under the same test condition. The Fe/N@CNF-800 of $E_{1/2}$ only shows slight negative shift (~12 mV) after 10000 CV cycles measurements, further demonstrating the super stability of Fe/N@CNF-800 catalyst (Fig. 4(f)).

Besides, as shown in Fig. 5, the ORR catalytic activity of Fe/N@CNFs catalysts in acidic medium was further studied. In the presence of 0.5 mol·L^{-1} O_2-saturated H_2SO_4 electrolyte, a series of obvious reduction peaks were observed (Fig. S16, cf. ESM). The LSV curves, as illustrated in Fig. 5(a), show much higher $E_{1/2}$ of Fe/N@CNF-800 (0.77 V) compared to that of Fe/N@CNF-700 (0.62 V), Fe/N@CNF-900 (0.71 V) and which is even very close to that of commercial Pt/C catalyst (0.79 V). In addition, Fe/N@CNF-800 (12.3 mA·cm^{-2}) also outperforms other catalysts in terms of J_k value (Fig. 5(b)). It is noteworthy that even under acidic condition, the Fe/N@CNF-800 shows better ORR catalytic activity compared to that of most recently reported acidic ORR electrocatalysts (as shown in Table S3, cf. ESM). The electron transfer numbers obtained from the K–L plots in acidic electrolyte for Fe/N@CNF-800 (Fig. 5(c)) are also in the range of 3.91–3.96 at 0.3–0.7 V (Fig. 5(d)), implying identical $4e^-$ transfer approach [45]. The chronoamperometric measurements clearly indicate much better durability of Fe/N@CNF-800 compared to that of the commercial Pt/C catalyst (Figs. 5(e) and 5(f)). The enhanced ORR durability of Fe/N@CNF-800 in acidic condition may be ascribed to the encapsulated Fe–N_x nanoparticles by carbon layers, which prevents the degradation of corresponding catalytic active centers [46–48]. Table 2 summarizes the electrocatalytic properties for the as-designed catalysts both under alkaline and acidic environment. Besides, among various recently reported Fe-based electrocatalysts, the as synthesized Fe/N@CNF-800 catalyst ranks high in terms of the ORR performance (Table S3).

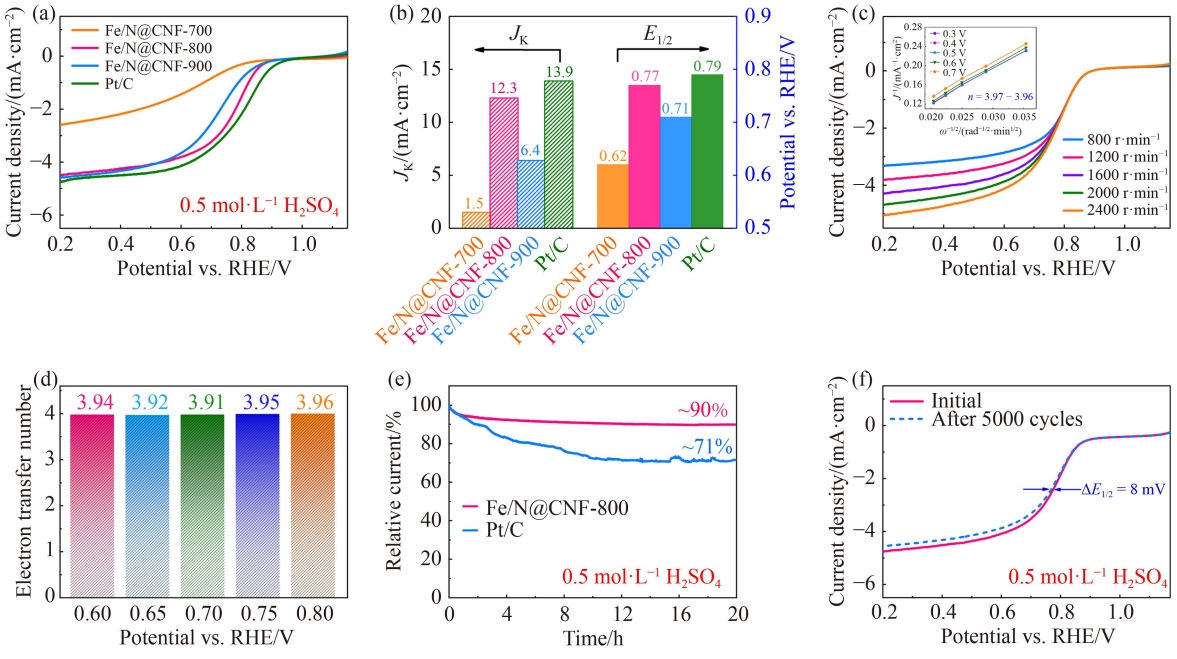

Fig. 5 (a) LSV curves of the Fe/N@CNFs and Pt/C catalysts in O_2-saturated 0.5 mol·L^{-1} H_2SO_4, respectively; (b) J_K and $E_{1/2}$ values of the Fe/N@CNFs and Pt/C catalysts, respectively; (c) LSV curves of Fe/N@CNF-800 catalyst at various rotating speeds, inset of (c) is K–L plots of Fe/N@CNF-800 catalyst at various potentials; (d) electron transfer number (*n*) of Fe/N@CNF-800 catalysts calculated from corresponding K–L equation; (e) chronoamperometric responses of Fe/N@CNF-800 and Pt/C catalysts in O_2-saturated 0.5 mol·L^{-1} H_2SO_4 at 0.664 V, respectively; (f) the LSV curves of Fe/N@CNF-800 before and after 5000 CV cycles.

The prominent ORR catalytic activity of Fe/N@CNF-800 can be ascribed primarily to the following perspectives: First, the electronic structure of carbon matrix can be effectively modulated due to the incorporation of Fe and N elements into the orderly carbon network which promote the adsorption and desorption of active intermediates during the ORR process; Second, by exposing high-density active centers which promote active mass transfer, the uniform nanofloret-like nano-architecture plays a significant role in optimizing the electrochemical/structural features; Third, the outward orderly graphitized carbon around the uniformly dispersed Fe–N_x nanoparticles ensures stable structures as well as prominent long-term stability.

Considering the outstanding ORR behavior of Fe/N@CNF-800 catalyst, its application in the field of energy conversion was investigated (Fig. 6). The practical implementation of the catalyst was evaluated by assembling a primary zinc–air battery (Fig. 6(a)). As can be seen from Fig. 6(b), at ~1.51 V, the steady open-circuit voltage (OCV) of the self-made zinc–air battery surpasses that of the commercial Pt/C catalyst (~1.50 V) [49]. In addition, two zinc–air batteries obtained by employing the Fe/N@CNF-800 cathode were capable of lighting up a green LED lamp overnight, indicating the possibility of applying Fe/N@CNF-800 in practical applications [50]. Noticeably, Fe/N@CNF-800 shows a high-power density of ~164 mW·cm^{-2} as obtained from the polarization

Table 2 ORR performance of Fe/N@CNFs and Pt/C catalysts in different pH environments

Sample	E_{onset}/(V vs. RHE)	$E_{1/2}$/(V vs. RHE)	J_L/(mA·cm^{-2})	Electrolyte
Fe/N@CNF-700	0.95	0.82	3.40	0.1 mol·L^{-1} KOH
	0.85	0.62	2.59	0.5 mol·L^{-1} H_2SO_4
Fe/N@CNF-800	1.02	0.89	5.15	0.1 mol·L^{-1} KOH
	0.92	0.78	4.48	0.5 mol·L^{-1} H_2SO_4
Fe/N@CNF-900	0.98	0.87	4.24	0.1 mol·L^{-1} KOH
	0.93	0.71	4.59	0.5 mol·L^{-1} H_2SO_4
Pt/C	1.01	0.86	4.88	0.1 mol·L^{-1} KOH
	0.98	0.79	4.78	0.5 mol·L^{-1} H_2SO_4

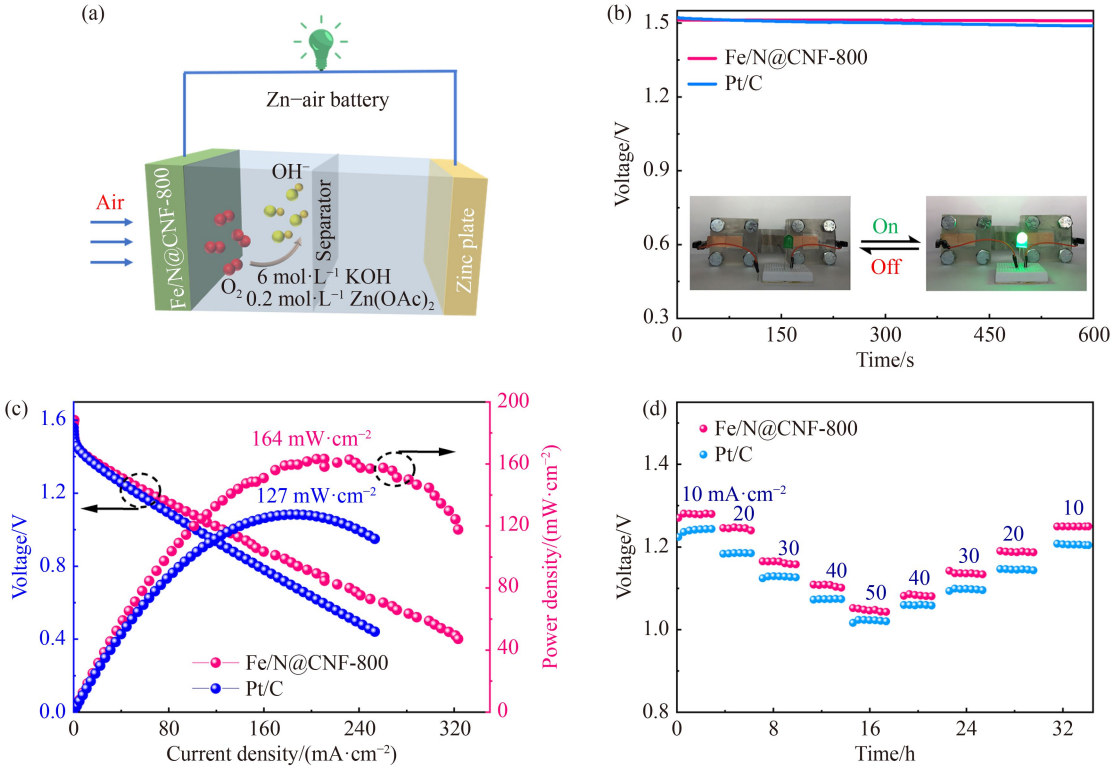

Fig. 6 (a) Schematic illustration of the zinc–air battery; (b) OCV curves of the zinc–air batteries with Fe/N@CNF-800 and Pt/C cathodes, respectively; (c) discharge polarization curves and the power density curves of zinc–air batteries with Fe/N@CNF-800 and Pt/C cathodes, respectively; (d) rate performance of Fe/N@CNF-800 and Pt/C electrodes at a current density of 10, 20, 30, 40, 50, and 10 mA·cm^{-2}, respectively.

curve (Fig. 6(c)), exceeding that of commercial Pt/C catalyst (~127 mW·cm^{-2}) and most of the reported catalysts (Table S4, cf. ESM). Furthermore, the rate performance of self-made zinc–air battery utilizing Fe/N@CNF-800 air-electrode was also found to be superior compared to that of the commercial Pt/C-based air-electrode (Fig. 6(d)). Above results clearly demonstrate that the Fe/N@CNF-800 electrocatalyst is a highly competitive candidate to supersede commercial Pt/C catalyst.

4 Conclusions

In summary, an inventive hypersaline confinement conversion strategy is reported to fabricate Fe/N@CNFs from a Fe-CTP. The sealing and capillary effect of NaCl molten salt facilitates the formation of Fe–N_x nanoparticles and nanosheets-assembled nanoflorets. As a result, the optimal Fe/N@CNF-800 exhibited a unique nanofloret structures, large specific surface area (~673.2 $m^2 \cdot g^{-1}$) and high doping content of N and Fe element (~4.84 and 0.99 at %). These unique characteristics enabled Fe/N@CNF-800 with high electrocatalytic performance as well superb durability towards the ORR in both alkaline and acidic conditions. As a demonstration, the self-assembled zinc–air battery using Fe/N@CNF-800 as cathode material delivers an ultrahigh peak powder density of 164 mW·cm^{-2} along with great rate performance. This work indicates that pyrolysis of transition metal coordinated CTPs can become an ideal method to prepare high-performance electrocatalysts for high-efficiency energy conversion application.

Acknowledgment The authors are grateful for the financial support from the National Natural Science Foundation of China (Grant Nos. 51872147 and 22006131).

Electronic Supplementary Material Supplementary material is available in the online version of this article at https://dx.doi.org/10.1007/s11705-022-2232-5 and is accessible for authorized users.

References

1. Wang Y J, Zhao N, Fang B, Li H, Bi X T, Wang H. Carbon-supported Pt-based alloy electrocatalysts for the oxygen reduction reaction in polymer electrolyte membrane fuel cells: particle size, shape, and composition manipulation and their impact to activity. Chemical Reviews, 2015, 115(9): 3433–3467
2. Shao M H, Chang Q W, Dodelet J P, Chenitz R. Recent advances in electrocatalysts for oxygen reduction reaction. Chemical Reviews, 2016, 116(6): 3594–3657
3. Jiao Y, Zheng Y, Jaroniec M, Qiao S Z. Design of electrocatalysts for oxygen- and hydrogen-involving energy conversion reactions. Chemical Society Reviews, 2015, 44(8): 2060–2086
4. Kang G S, Lee G, Cho S Y, Joh H I, Lee D C, Lee S. Recycling of waste tires by synthesizing N-doped carbon-based catalysts for oxygen reduction reaction. Applied Surface Science, 2021, 548: 149027–149031
5. Ge F, Qiao Q G, Chen X, Wu Y. Probing the catalytic activity of M-N_4-xO_x embedded graphene for the oxygen reduction reaction by density functional theory. Frontiers of Chemical Science and Engineering, 2021, 15(5): 1206–1216
6. Sun J, Guo N K, Song T S, Hao Y R, Sun J W, Xue H, Wang Q. Revealing the interfacial electron modulation effect of CoFe alloys with CoC_x encapsulated in N-doped CNTs for superior oxygen reduction. Advanced Powder Materials, 2022, 1(3): 100023–100029
7. Peng J H, Tao P, Song C Y, Shang W, Deng T, Wu J B. Structural evolution of Pt-based oxygen reduction reaction electrocatalysts. Chinese Journal of Catalysis, 2022, 43(1): 47–58
8. Peng W, Yang X X, Mao L C, Jin J H, Yang S L, Zhang J J, Li G. ZIF-67-derived Co nanoparticles anchored in N doped hollow carbon nanofibers as bifunctional oxygen electrocatalysts. Chemical Engineering Journal, 2021, 407: 127157–127167
9. Han J X, Bao H L, Wang J Q, Zheng L R, Sun S R, Wang Z L, Sun C W. 3D N-doped ordered mesoporous carbon supported single-atom Fe–N–C catalysts with superior performance for oxygen reduction reaction and zinc–air battery. Applied Catalysis B: Environmental, 2021, 280: 119411–119420
10. Pan Y L, Liu S, Sun K, Chen X, Wang B, Wu K, Cao X, Cheong W C, Shen R, Han A, Chen Z, Zheng L, Luo J, Lin Y, Liu Y, Wang D, Peng Q, Zhang Q, Chen C, Li Y. A bimetallic Zn/Fe polyphthalocyanine-derived single-atom Fe–N_4 catalytic site: a superior trifunctional catalyst for overall water splitting and Zn–air batteries. Angewandte Chemie International Edition, 2018, 57(28): 8614–8618
11. Yang Z, Yan X, Tang Z, Peng W, Zhang J, Tong Y, Li J, Zhang J. Facile synthesis of hemin-based Fe–N–C catalyst by MgAl-LDH confinement effect for oxygen reduction reaction. Applied Surface Science, 2022, 573: 151505–151513
12. Qiao M, Wang Y, Wang Q, Hu G, Mamat X, Zhang S, Wang S. Hierarchically ordered porous carbon with atomically dispersed Fe–N_4 for ultraefficient oxygen reduction reaction in proton-exchange membrane fuel cells. Angewandte Chemie International Edition, 2020, 59(7): 2688–2694
13. Zheng Y, Song H, Chen S, Yu X H, Zhu J X, Xu J S, Zhang K A I, Zhang C, Liu T. Metal-free multi-heteroatom-doped carbon bifunctional electrocatalysts derived from a covalent triazine polymer. Small, 2020, 16(47): 2004342–2004352
14. Yu X H, Zheng Y, Zhang H P, Wang Y F, Fan X S, Liu T X. Fast-recoverable, self-healable, and adhesive nanocomposite hydrogel consisting of hybrid nanoparticles for ultrasensitive strain and pressure sensing. Chemistry of Materials, 2021, 33(15): 6146–6157
15. Yu X H, Zheng Y, Wang Y F, Zhang H P, Song H, Li Z B, Fan X S, Liu T X. Facile fabrication of highly stretchable, stable, and self-healing ion-conductive sensors for monitoring human motions. Chemistry of Materials, 2022, 34(3): 1110–1120
16. Xu J, Zhu C, Song S, Fang Q, Zhao J, Shen Y. A nanocubicle-like 3D adsorbent fabricated by *in situ* growth of 2D heterostructures

for removal of aromatic contaminants in water. Journal of Hazardous Materials, 2022, 423: 127004–127012

17. Ding F, Yu Z, Chen X, Chen X, Chen C, Huang Y, Yang Z, Zou C, Yang K, Huang S. High-performance supercapacitors based on reduced graphene oxide-wrapped carbon nanoflower with efficient transport pathway of electrons and electrolyte ions. Electrochimica Acta, 2019, 306: 549–557
18. Li H, Du K, Xiang C, An P, Shu X, Dang Y, Wu C, Wang J, Du W, Zhang J, Li S, Tian H, Wang S, Xia H. Controlled chelation between tannic acid and Fe precursors to obtain N, S co-doped carbon with high density Fe-single atom-nanoclusters for highly efficient oxygen reduction reaction in Zn–air batteries. Journal of Materials Chemistry A: Materials for Energy and Sustainability, 2020, 8(33): 17136–17149
19. Gan Z, Shu C, Deng C, Du W, Huang B, Tang W. Confinement of Pt NPs by hollow-porous-carbon-spheres via pore regulation with promoted activity and durability in the hydrogen evolution reaction. Nanoscale, 2021, 13(43): 18273–18280
20. Shu C, Tan Q, Deng C, Du W, Gan Z, Liu Y, Fan C, Jin H, Tang W, Yang X, Yang X, Wu Y. Hierarchically mesoporous carbon spheres coated with a single atomic Fe–N–C layer for balancing activity and mass transfer in fuel cells. Carbon Energy, 2022, 4(1): 1–11
21. Chung D Y, Yoo J M, Sung Y. Highly durable and active Pt-based nanoscale design for fuel-cell oxygen-reduction electrocatalysts. Advanced Materials, 2018, 30(42): 1704123–1704142
22. Zong W, Chui N B, Tian Z H, Li Y Y, Yang C, Rao D W, Wang W, Huang J J, Wang J T, Lai F, Liu T. Ultrafine MoP nanoparticle splotched nitrogen-doped carbon nanosheets enabling high-performance 3D-printed potassium-ion hybrid capacitors. Advanced Science, 2021, 8(7): 2004142–2004152
23. Kamiya K. Selective single-atom electrocatalysts: a review with a focus on metal-doped covalent triazine frameworks. Chemical Science, 2020, 11(32): 8339–8349
24. Jiao L, Hu Y, Ju H, Wang C, Gao M R, Yang Q, Zhu J, Yu S H, Jiang H L. From covalent triazine-based frameworks to N-doped porous carbon/reduced graphene oxide nanosheets: efficient electrocatalysts for oxygen reduction. Journal of Materials Chemistry A: Materials for Energy and Sustainability, 2017, 5(44): 23170–23178
25. He Y, Gehrig D, Zhang F, Lu C, Zhang C, Cai M, Wang Y, Laquai F, Zhuang X, Feng X. Highly efficient electrocatalysts for oxygen reduction reaction based on 1D ternary doped porous carbons derived from carbon nanotube directed conjugated microporous polymers. Advanced Functional Materials, 2016, 26(45): 8255–8265
26. Ma Y, Chen W, Jiang Z, Tian X, Guo X, Chen G, Jiang Z J. NiFe-nanoparticles supported on N-doped graphene hollow spheres entangled with self-grown N-doped carbon nanotubes for liquid electrolyte/flexible all-solid-state rechargeable zinc–air batteries. Journal of Materials Chemistry A: Materials for Energy and Sustainability, 2022, 10(23): 12616–12631
27. Zheng Y, Chen S, Zhang K A I, Guan J, Yu X, Peng W, Song H, Zhu J, Xu J, Fan X, Zhang C, Liu T. Template-free construction of hollow mesoporous carbon spheres from a covalent triazine framework for enhanced oxygen electroreduction. Journal of Colloid and Interface Science, 2022, 608: 3168–3177
28. Wang W, Chen W, Miao P, Luo J, Wei Z, Chen S. NaCl crystallites as dual-functional and water-removable templates to synthesize a three-dimensional graphene-like macroporous Fe–N–C catalyst. ACS Catalysis, 2017, 7(9): 6144–6149
29. Zheng Y, Qing F L, Huang Y, Xu X H. Tunable and practical synthesis of thiosulfonates and disulfides from sulfonyl chlorides in the presence of tetrabutylammonium iodide. Advanced Synthesis & Catalysis, 2016, 358(21): 3477–3481
30. Zhu C, Fang Q, Liu R, Dong W, Song S, Shen Y. Insights into the crucial role of electron and spin structures in heteroatom-doped covalent triazine frameworks for removing organic micropollutants. Environmental Science & Technology, 2022, 56(10): 6699–6709
31. Chen S, Zheng Y, Zhang B, Feng Y, Zhu J, Xu J, Zhang C, Feng W, Liu T. Cobalt, nitrogen-doped porous carbon nanosheet-assembled flowers from metal-coordinated covalent organic polymers for efficient oxygen reduction. ACS Applied Materials & Interfaces, 2019, 11(1): 1384–1393
32. Zhang X, Mollamahale Y B, Lyu D, Liang L, Yu F, Qing M, Du Y, Zhang X, Tian Z Q, Shen P K. Molecular-level design of Fe–N–C catalysts derived from Fe-dual pyridine coordination complexes for highly efficient oxygen reduction. Journal of Catalysis, 2019, 372: 245–257
33. Zhao X, Pachfule P, Li S, Langenhahn T, Ye M, Tian G, Schmidt J, Thomas A. Silica-templated covalent organic framework-derived Fe-N-doped mesoporous carbon as oxygen reduction electrocatalyst. Chemistry of Materials, 2019, 31(9): 3274–3280
34. Ding W, Li L, Xiong K, Wang Y, Li W, Nie Y, Chen S, Qi X, Wei Z. Shape fixing via salt recrystallization: a morphology-controlled approach to convert nanostructured polymer to carbon nanomaterial as a highly active catalyst for oxygen reduction reaction. Journal of the American Chemical Society, 2015, 137(16): 5414–5420
35. Zheng Y, Chen S, Yu X, Li K, Ni X, Ye L. Nitrogen-doped carbon spheres with precisely-constructed pyridinic-N active sites for efficient oxygen reduction. Applied Surface Science, 2022, 598: 153786–153793
36. Zheng Y, Ni X, Li K, Yu X, Song H, Chen S, Khan N A, Wang D, Zhang C. Multi-heteroatom-doped hollow carbon nanocages from ZIF-8@CTP nanocomposites as high-performance anodes for sodium-ion batteries. Composites Communications, 2022, 32: 101116–101122
37. Zong W, Guo H, Ouyang Y, Mo L, Zhou C, Chao G, Hofkens J, Xu Y, Wang W, Miao Y E, He G, Parkin I P, Lai F, Liu T. Topochemistry-driven synthesis of transition-metal selenides with weakened van der Waals force to enable 3D-printed Na-ion hybrid capacitors. Advanced Functional Materials, 2022, 32(13): 2110016–2110025
38. Zhang X, Wang F, Dou L, Cheng X, Si Y, Yu J, Ding B. Ultrastrong, superelastic, and lamellar multiarch structured ZrO_2-Al_2O_3 nanofibrous aerogels with high-temperature resistance over 1300 °C. ACS Nano, 2020, 14(11): 15616–15625
39. Liu S, Xu J, Zhu J, Chang Y, Wang H, Liu Z, Xu Y, Zhang C, Liu T. Leaf-inspired interwoven carbon nanosheet/nanotube

homostructures for supercapacitors with high energy and power densities. Journal of Materials Chemistry A: Materials for Energy and Sustainability, 2017, 5(37): 19997–20004

40. Fan F, Zhou H, Yan R, Yang C, Zhu H, Gao Y, Ma L, Cao S, Cheng C, Wang Y. Anchoring Fe–N–C sites on hierarchically porous carbon sphere and CNT interpenetrated nanostructures as efficient cathodes for zinc–air batteries. ACS Applied Materials & Interfaces, 2021, 13(35): 41609–41618
41. Unni S M, Devulapally S, Karjule N, Kurungot S. Graphene enriched with pyrrolic coordination of the doped nitrogen as an efficient metal-free electrocatalyst for oxygen reduction. Journal of Materials Chemistry, 2012, 22(44): 23506–23513
42. Xing Z, Jin R, Chen X, Chen B, Zhou J, Tian B, Li Y, Fan D. Self-templating construction of N, P-co-doped carbon nanosheets for efficient eletreocatalytic oxygen reduction reaction. Chemical Engineering Journal, 2021, 410: 128015–128020
43. Zhu T, Feng Q, Liu S, Zhang C. Metallogel-derived 3D porous carbon nanosheet composites as an electrocatalyst for oxygen reduction reaction. Composites Communications, 2020, 20: 100376–100380
44. Zheng Y, Chen S, Zhang K, Zhu J, Xu J, Zhang C, Liu T. Ultrasound-triggered assembly of covalent triazine framework for synthesizing heteroatom-doped carbon nanoflowers boosting metal-free bifunctional electrocatalysis. ACS Applied Materials & Interfaces, 2021, 13(11): 13328–13337
45. Zhang R Q, Ma A, Liang X, Zhao L M, Zhao H, Yuan Z Y. Cobalt nanoparticle decorated N-doped carbons derived from a cobalt covalent organic framework for oxygen electrochemistry. Frontiers of Chemical Science and Engineering, 2021, 15(6): 1550–1560
46. Zhang S, Liu X, Li Z, Hao L, Wang P, Zou X, Liu Z, Zhang G, Zhang C Y. Iron and iodine co-doped triazine-based frameworks with efficient oxygen reduction reaction in alkaline and acidic media. ACS Sustainable Chemistry & Engineering, 2019, 7(13): 11787–11794
47. Yuan K, Sfaelou S, Qiu M, Lützenkirchen-Hecht D, Zhuang X, Chen Y, Yuan C, Feng X, Scherf U. Synergetic contribution of boron and Fe–N_x species in porous carbons toward efficient electrocatalysts for oxygen reduction reaction. ACS Energy Letters, 2018, 3(1): 252–260
48. Zheng Y, Chen S, Lu H, Zhang C, Liu T. 3D honeycombed cobalt, nitrogen co-doped carbon nanosheets via hypersaline-protected pyrolysis towards efficient oxygen reduction. Nanotechnology, 2020, 31(36): 364003
49. Zheng Y, Chen S, Song H, Guo H, Zhang K A I, Zhang C, Liu T. Nitrogen-doped hollow carbon nanoflowers from a preformed covalent triazine framework for metal-free bifunctional electrocatalysis. Nanoscale, 2020, 12(27): 14441–14447
50. Guan C, Sumboja A, Zang W, Qian Y, Zhang H, Liu X, Liu Z, Zhao D, Pennycook S J, Wang J. Decorating Co/CoN_x nanoparticles in nitrogen-doped carbon nanoarrays for flexible and rechargeable zinc–air batteries. Energy Storage Materials, 2019, 16: 243–250